Eur. Phys. J. Plus (2021) 136:783
https://doi.org/10.1140/epjp/s13360-021-01793-2

THE EUROPEAN PHYSICAL JOURNAL PLUS

Regular Article

Flow field analysis of an elliptical moving belt in transitional flow regime

Erfan Salimipour[1], **Shima Yazdani**[1], **Mohammad Ghalambaz**[2,3,a]

[1] Department of Mechanical Engineering, Quchan University of Technology, 94771-77870 Quchan, Iran
[2] Metamaterials for Mechanical, Biomechanical and Multiphysical Applications Research Group, Ton Duc Thang University, Ho Chi Minh City 758307, Vietnam
[3] Faculty of Applied Sciences, Ton Duc Thang University, Ho Chi Minh City 758307, Vietnam

Received: 21 May 2021 / Accepted: 22 July 2021

Abstract Study on complicated flows around bluff bodies is significant in terms of flow physics and various engineering applications. In the current paper, a simulation of the flow past an elliptical moving belt along with the Magnus effect in a transitional flow regime was performed. The angle of attack and rotational speed of the moving belt were considered as the variable parameters at a fixed Reynolds number of 10^5 and ellipse axis ratio (minor to major diameter ratio) of 0.25. The belt motion was such that the ellipse's upper surface was moved in the same direction of the flow and the lower surface motion was in the opposite direction. The numerical simulation procedure was based on the discretization of two-dimensional Reynolds-averaged Navier–Stokes equations using a pressure-based solver. A modified version of the k-k_L-ω turbulence model with the ability to predict separation bubbles was utilized. A large eddy simulation (LES) was also performed to ensure the validity of the two-dimensional assumption and the utilized turbulence model. Results indicated that the belt motion led to a decrease in the boundary layer thickness on the upper surface and an increase in the boundary layer thickness on the belt's lower surface. Moreover, as the attack angle increased, the turbulence on the upper and lower surfaces increased and decreased, respectively. The aerodynamic analysis showed that the belt motion enhanced the lift coefficient and reduced the elliptical belt drag coefficient.

1 Introduction

Generating the lift force via fluid flow is one of the main goals of fluid dynamics and aerodynamics. This force is commonly generated by airfoils; however, in some special applications, a bluff body may be used. In symmetric bluff bodies such as circular cylinders, the mean lift force is zero. In these cases, the rotation of the cylinder can result in a lift force due to the Magnus effect. Research studies have shown that the flow past a rotating cylinder can be very complex. Several classifications for the flow patterns have been presented in [1–6]. On the other hand, an elliptical cylinder under an angle of attack generates the lift force.

[a] e-mail: mohammad.ghalambaz@tdtu.edu.vn (corresponding author)

Various research studies on the flow around elliptical cylinders have been carried out so far. Mittal and Balachandar [7] numerically simulated the flow around several elliptical cylinders with different axis ratios and a range of Reynolds numbers between 180 and 1000. They compared their two- and three-dimensional results with experimental data. Khan et al. [8] analytically studied the flow and heat transfer of an elliptical cylinder, assuming the two-dimensional, steady, and laminar flow for various ranges of the Reynolds numbers, Prandtl numbers, and axis ratios. Paul et al. [9] numerically studied the flow past unconfined two-dimensional elliptical cylinders to anticipate the vortex shedding and flow separation. In the article for different axis ratios and angles of attack, the critical Reynolds number and Strouhal number have been predicted. Moreover, Paul et al. [10] numerically studied the flow past an elliptical cylinder in the laminar regime for the Reynolds numbers of 50, 100 150, and 200, a range of axis ratios between 0.1 and 1 the angles of attack ranging from 30 to 90^{o}. They analyzed the flow pattern, drag coefficient, and Strouhal numbers by varying the above-mentioned parameters. Furthermore, Thompson et al. [11] numerically studied the flow wakes behind the several elliptic cylinders with a range of axis ratios from 0 to 1 and Reynolds numbers between 50 and 200 in two- and three-dimensional conditions. Subburaj et al. [12] studied the flow around an elliptical cylinder with different axis ratios and angles of attack. The flow patterns and bulk parameters included the aerodynamic forces and Strouhal number were also investigated. The results revealed that by increasing the axis ratio, the mean forces increased and Strouhal number decreased. Ezadi Yazdi and Bak Khoshnevis [13] experimentally studied the flow around an elliptical cylinder at two Reynolds numbers 1.5×10^4 and 3×10^4. Their results showed that with increasing the Reynolds number, the turbulence intensity in the near-wake zone decreased.

Several studies have also been performed about the flow past rotating circular and elliptical cylinders. Jiang et al. [14] numerically investigated wake transitions of flow past a circular cylinder near a moving wall for two- and three-dimensional at the Reynolds numbers up to 300. Because of the presence of the wall, the critical Reynolds number decreased for the two-dimensional flow. They concluded that the vortex shedding delayed due to the weak interaction between the vortices shed from the cylinder's top and bottom parts. Naik et al. [15] carried out a numerical simulation for the flow around a rotating elliptical cylinder with counter-clockwise rotation at Reynolds number based on the cylinder perimeter of 100 for the rotation rates of 0.5, 1, and 1.5 and a range of axis ratios between 0.1 and 1. They analyzed the flow patterns and lift and drag coefficients. Moreover, they [16] investigated the shear flow effects on stationary and rotating elliptic cylinders. Lu et al. [17] also studied the flow past rotating elliptical cylinders for a range of axis ratios from 0.0625 to 1 and the higher rotation rates of 3, 4, 4.6, and 5 at the Reynolds number of 200. Zhu et al. [18] investigated the flow over an elliptical cylinder near a moving wall for Reynolds numbers less than 150 with an axis ratio of 0.4. They presented some insight into the physical process of transitional movements of bluff bodies near a stationary plane wall.

Investigations about moving surfaces (also known as moving wall or moving belt) were first carried out for the boundary layer control [19]. Moktarian and Modi [20] experimentally and numerically investigated the effects of placing a rotating cylinder on the leading edge of the Joukowsky airfoil as a moving surface boundary layer control at $\mathrm{Re} = 2.3 \times 10^5$. In the continuing study [21], they placed a second rotating cylinder on the upper surface of the airfoil. Their results showed that the use of two rotating cylinders, in addition to delaying the stall, provided an extra lift than the use of a single rotating cylinder. This mechanism could delay the flow separation by injecting the momentum into the boundary layer [22, 23] with little energy input [24]. Boukenkoul et al. [25] experimentally investigated the effect of a moving belt on the flow past a thick airfoil. Their results showed the upper surface flow

reattachment and also a significant increase in the lift coefficient. Salimipour and Salimipour [26] used a pair of moving surfaces on a circular cylinder in a laminar flow regime to control the vortex shedding and reduce the drag force and power consumption. They found the speed and location of the moving surfaces, which led to minimizing the power consumption. Furthermore, Salimipour and Yazdani [27] numerically studied the moving wall effect on the performance of a wind turbine blade at $\mathrm{Re} = 7.5 \times 10^5$ and a range of angle of attack between 5 and 28°. They could enhance the power generation of the turbine, especially at lower tip speed ratios.

In addition to the aspects mentioned above, a transition from laminar to turbulent flow and laminar separation bubble (LSB) formation may affect the flow field and aerodynamic characteristics. For an airfoil, LSB is categorized into a short and long bubble. As the angle of attack increases, the short bubble shrinks and moves toward the leading edge. With a further increment in the attack angle, the short bubble cannot reattach to the airfoil surface. Consequently, the short bubble bursts and this leads to the occurrence of airfoil stall [28]. In this situation, a long separation bubble is formed, covering the entire upper surface of the airfoil. These bubbles can appear in a range of Reynolds numbers from 3×10^4 to 7×10^5. Due to the complexity of the numerical simulation of the transitional flows, various research studies have been done in this field [29–33].

Although the combined impacts of the interaction of the Magnus effect, attack angle, blunt body, momentum injection, and laminar separation bubble in a transitional flow regime can be important both in terms of flow physics and industrial applications, it has not been studied so far. These combined impacts may occur in small-sized wind and marine turbines, microair vehicles, and also a part of the flow control mechanism. In the current paper, a numerical investigation of the flow field around an elliptical moving belt in the transitional flow regime and the analysis of the lift and drag coefficients are carried out. A study on the above-mentioned combined effects is the major novelty of the paper. The ellipse axis ratio (minor to major diameter ratio) is 0.25, and the Reynolds number based on the major diameter is 10^5. The ratio of belt speed to free-stream velocity (k) between 0 and 2 and the angles of attack ranging from 0 to 30° is considered. Two configurations are considered as shown in Fig. 1. For the full belt configuration, the ellipse's upper surface moves in the same direction of the flow, and the lower surface motion is in the opposite direction. For the half belt configuration, only the upper surface moves, while the ellipse's lower surface is stationary.

The present study focuses on the following objectives:

- Numerical simulation and validation of the transitional flow past an elliptical moving belt
- Analysis of the lift and drag coefficients of the elliptical moving belt
- Investigation of the speed ratio (k) impact on the flow field and stall angle
- Study on the formation and position of the laminar separation bubble
- Classification of the flow patterns around the elliptical belt

2 Mathematical and numerical formulation

In this study, a numerical solution of the two-dimensional Navier–Stokes equations is carried out to simulate the flow field using an in-house finite-volume pressure-based solver. Differential forms of the continuity and momentum equations for a two-dimensional and incompressible flow can be written as follows:

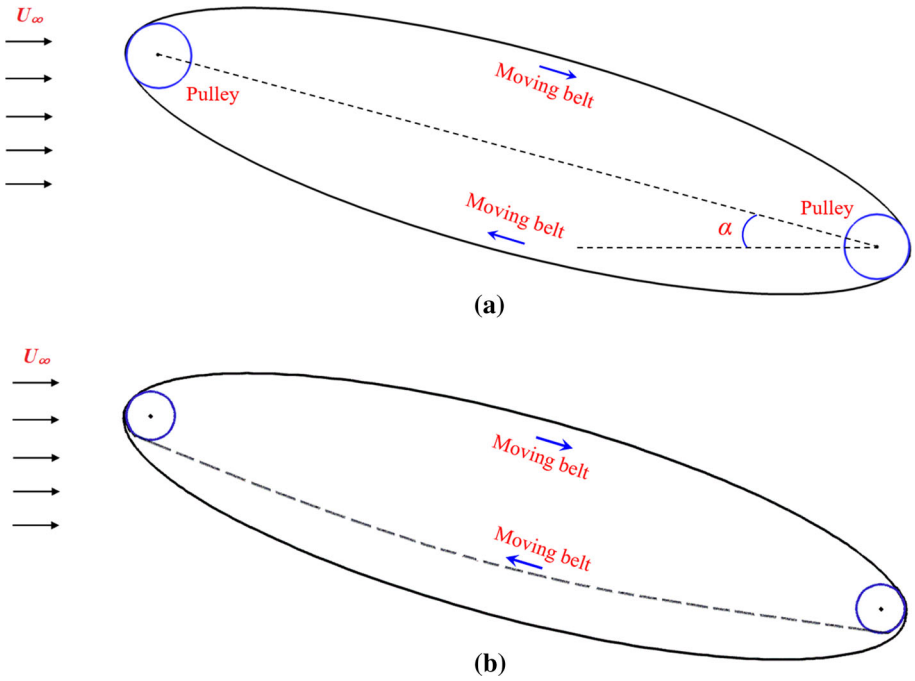

Fig. 1 Configurations of elliptical moving belt under an angle of attack **a** full belt, **b** half belt

$$\frac{\partial u}{\partial x}+\frac{\partial v}{\partial y}=0 \tag{1}$$

$$\frac{\partial u}{\partial t}+u\frac{\partial u}{\partial x}+v\frac{\partial u}{\partial y}=-\frac{1}{\rho}\frac{\partial p}{\partial x}+(\nu+\nu_t)\left(\frac{\partial^2 u}{\partial x^2}+\frac{\partial^2 u}{\partial y^2}\right) \tag{2}$$

$$\frac{\partial v}{\partial t}+u\frac{\partial v}{\partial x}+v\frac{\partial v}{\partial y}=-\frac{1}{\rho}\frac{\partial p}{\partial y}+(\nu+\nu_t)\left(\frac{\partial^2 v}{\partial x^2}+\frac{\partial^2 v}{\partial y^2}\right) \tag{3}$$

where ρ is the fluid density, υ and υ_t denote the kinematic and turbulent viscosity, respectively, and t is the flow time. The velocity variables (u and v) and pressure (p) are the Reynolds-averaged quantities. To achieve the turbulent viscosity (υ_t) for transitional flows, a version of the three-equation k-k_L-ω turbulence model modified by Salimipour [32] is utilized. The transport equations of this model are written as follows:

$$\frac{Dk_T}{Dt}=P_{k_T}+R_{BP}+R_{NAT}-\omega k_T-D_T+\frac{\partial}{\partial x_j}\left[\left(\nu+\frac{\alpha_T}{\sigma_k}\right)\frac{\partial k_T}{\partial x_j}\right] \tag{4}$$

$$\frac{Dk_L}{Dt}=P_{k_L}-R_{BP}-R_{NAT}-D_L+\frac{\partial}{\partial x_j}\left[\nu\frac{\partial k_L}{\partial x_j}\right] \tag{5}$$

$$\begin{aligned}\frac{D\omega}{Dt}&=C_{\omega 1}\frac{\omega}{k_T}P_{k_T}+\left(\frac{C_{\omega R}}{f_W}-1\right)\frac{\omega}{k_T}(R_{BP}+R_{NAT})-f_W^2 C_{\omega 2}\omega^2\\&\quad+C_{\omega 3}f_\omega\alpha_T f_W^2\frac{\sqrt{k_T}}{d^3}+\frac{\partial}{\partial x_j}\left[\left(\nu+\frac{\alpha_T}{\sigma_\omega}\right)\frac{\partial\omega}{\partial x_j}\right]\end{aligned} \tag{6}$$

The variables used in Eqs. (4) to (6) include all of the terms that affected the flow transition and turbulence, which are detailed in [32]. This modified version has excellent accuracy in predicting the long and short laminar separation bubbles and stall onset. The turbulent intensity is assumed to be 0.1%.

An unsteady incompressible flow solver based on the Semi-Implicit Method for Pressure-Linked Equations (SIMPLE) is used for the flow simulations used in [26, 27, 32, 34]. A four-stage explicit Runge–Kutta method with second-order accuracy in time using the Crank–Nicholson scheme is applied to integrate Eqs. (2)–(6). The discretization of the convection terms of the above equations is performed using the second-order upwind scheme, while the viscous terms are discretized using the central scheme.

The solver output includes the pressure distribution, lift and drag coefficients as well as the streamlines and contours of the flow characteristics. The coefficients are obtained using the following relations:

$$C_{\mathrm{p}} = \frac{p - p_{\infty}}{1/2 \rho U_{\infty}^2} \tag{7}$$

$$C_{\mathrm{d}} = \frac{F_{\mathrm{d}}}{1/2 \rho U_{\infty}^2 c}; F_{\mathrm{d}} = \oint_{\partial \Omega} \left[n_{\mathrm{x}} \tau_{\mathrm{xy}} + n_{\mathrm{y}} \left(\tau_{\mathrm{yy}} - p \right) \right] dS \tag{8}$$

$$C_{\mathrm{l}} = \frac{F_l}{1/2 \rho U_{\infty}^2 c}; F_{\mathrm{l}} = \oint_{\partial \Omega} \left[n_{\mathrm{y}} \tau_{\mathrm{xy}} + n_{\mathrm{x}} (\tau_{\mathrm{xx}} - p) \right] dS \tag{9}$$

where F_{d} and F_{l} denote the lift and drag forces, c is the ellipse's primary diameter, dS is the surface element, and p_{∞} and U_{∞} are the free-stream pressure and free-stream velocity, respectively.

The performance of the moving belt is a function of the power consumption of the belt due to the fact that the moving belt consumes an external power. Therefore, along with the aerodynamic performance (Cl / Cd), the mechanical performance can be defined as follows [27]:

$$\eta = \frac{C_{\mathrm{l}}}{C_{\mathrm{d}} + C_{\mathrm{pc}}} \tag{10}$$

where C_{pc} represents the power consumption coefficient which is defined as follows:

$$C_{\mathrm{pc}} = k C_{f_{\mathrm{belt}}}; C_{f_{\mathrm{belt}}} = \frac{F_{f_{\mathrm{belt}}}}{1/2 \rho U_{\infty}^2 c} \tag{11}$$

where $F_{f_{belt}}$ is the moving belt's frictional force.

3 Generation of computational grid and boundary conditions

The present solver can be used on a structured grid. For this purpose, an orthogonal grid is generated with a non-dimensional wall distance of less than one ($y^+ < 1$). The numerical solution is performed on a circular domain having a diameter about 50 times the ellipse's preliminary diameter (c). Figure 2 shows a close-up view of the grid in x–y plane. The boundary conditions applied to the computational domain include a velocity inlet on the left half, a pressure outlet on the right half, and a solid boundary on the belt, as shown in Fig. 3. Furthermore, due to the low Reynolds number flow considered in the present study, the turbulence intensity applied to the free stream is $Tu_{\infty} = 0.1\%$. The inlet boundary conditions for k_T, k_L, and ω are given as follows [35]:

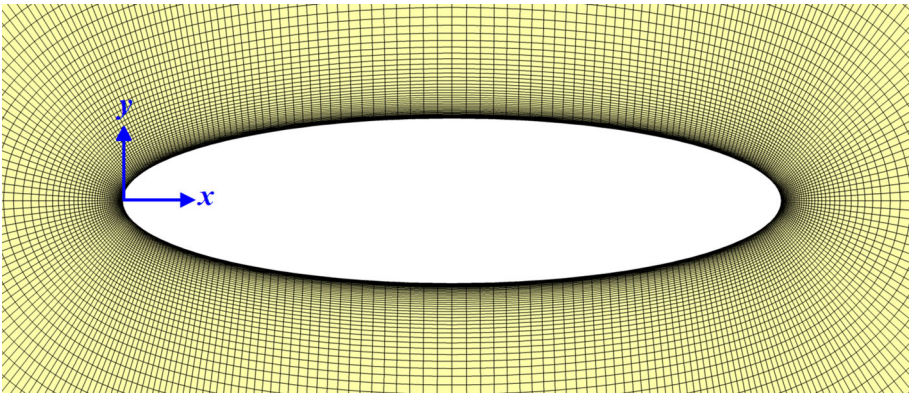

Fig. 2 A grid view utilized in the numerical simulation

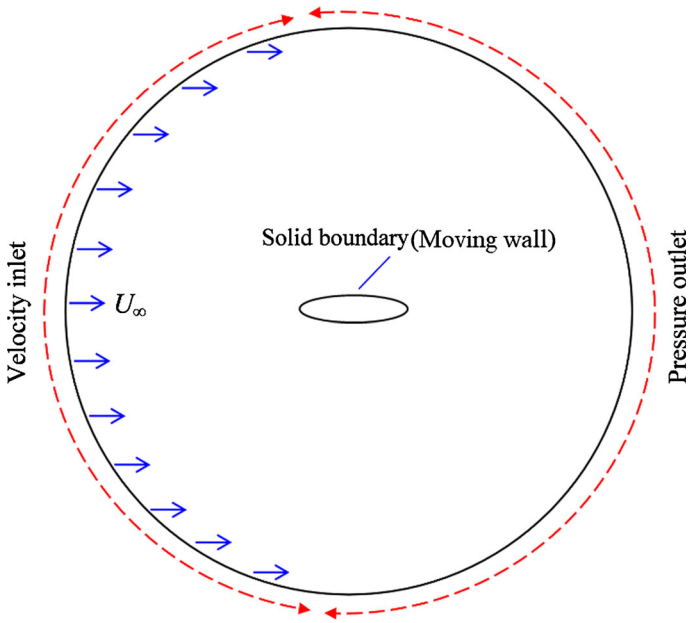

Fig. 3 Boundary conditions of the considered domain

$$k_T = \frac{3}{2}(TuU)^2_\infty;\ k_L = 0;\ \omega = \frac{0.09 k_T}{\nu_R \nu}$$

where ν_R is the ratio of turbulent to molecular viscosity at free stream.

Table 1 GCI calculations for lift and drag coefficients at $\alpha = 30°$, $\mathrm{Re} = 10^5$, and $k = 2$

	f_1 (coarse)	f_2 (medium)	f_3 (fine)	GCI_{12} (%)	GCI_{23} (%)
C_l	2.236	2.534	2.545	0.54	0.02
C_d	0.168	0.121	0.118	3.31	0.21

4 Results

4.1 Grid sensitivity and code validation study

The grid convergence index (GCI) methodology is utilized to estimate the uncertainty due to the grid spacing. For three grid resolutions of 1: coarse, 2: medium, and 3: fine, the GCI formulation based on Richardson's extrapolation theory can be written as follows [36]:

$$GCI_{i,i+1} = F_S \frac{|\varepsilon_{i,i+1}|}{r^p - 1};\ i = 1, 2, 3 \tag{12}$$

$$\varepsilon_{i,i+1} = \frac{f_i - f_{i+1}}{f_{i+1}} \tag{13}$$

$$p = \frac{ln|(f_1 - f_2)/(f_2 - f_3)|}{ln(r)} \tag{14}$$

where F_S, ε, r, p, and f denote the safety factor, relative error, grid refinement ratio, order of accuracy, and solution value, respectively. For three grids, $F_S = 1.25$ [36]. The lower the value of the GCI, the lower the grid sensitivity.

In the present study, three grids with 1: 285×85, 2: 400×120, and 3: 560×170 points on two directions with a constant $r = 1.4$ are considered. Two solution values of C_l and C_d are examined for the GCI study at $\alpha = 30°$, $\mathrm{Re} = 10^5$, axis ratio of 0.25, and speed ratio $k = \frac{U_{belt}}{U_\infty} = 2$. Table 1 presents the GCI calculations for the above-mentioned grids. Due to the low percentage of the GCI_{23}, the medium grid with 400×120 points is chosen for calculations.

Although the present numerical procedure has been previously validated in [26, 27, 32, 37], a number of new cases are also investigated in terms of the correspondence with experimental data and numerical results. Three cases are chosen to validate the LSB formation, flow around the elliptical cylinder, and two-dimensional flow assumption. Figure 4 depicts the comparison of the pressure coefficient distribution of the NACA 0025 airfoil between the present results and a large eddy simulation (LES) result and experimental data from [38] at the Reynolds number of 10^5 and $\alpha = 5°$. The obtained present results agree well with the experimental data. In particular, it has a better precision than the LES results to predict the transition from laminar to turbulent flow at $x/c = 0.5$.

The second case compares the distribution of pressure coefficient with the experimental data from [39] for an elliptical cylinder having an axis ratio of 1:3 at $\alpha = 15°$ and $\mathrm{Re} = 1.25 \times 10^5$. Figure 5 shows the comparison along with the region of transitional flow. A good agreement is obtained. The contours of turbulent kinetic energy (TKE) near the transition point and the LSB location are also depicted in Fig. 6. An increase in the TKE in a region that includes fluctuation leads to the separated boundary layer's reattachment.

Moreover, to ensure the validity of the two-dimensional assumption for the flow around the above-mentioned cylinder, a three-dimensional large eddy simulation is carried out for an elliptical moving belt using the Ansys fluent software. The grid used for simulation has $2000 \times 180 \times 50$ points on the tangential, radial, and depth directions, respectively. Figure 7

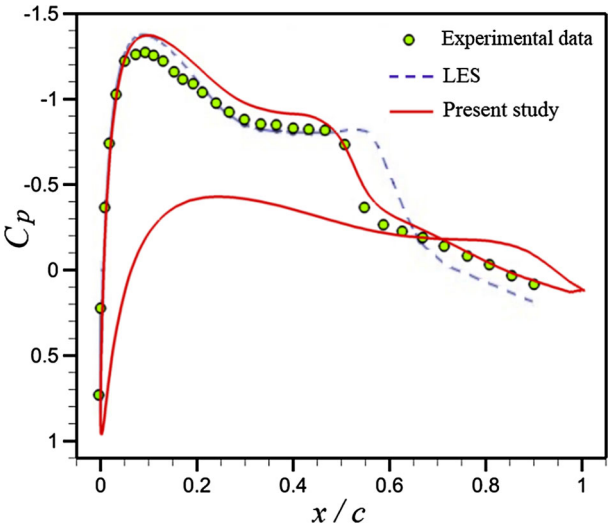

Fig. 4 Comparison of pressure coefficient of NACA 0025 airfoil with experimental and LES data at $\mathrm{Re} = 10^5$ and $\alpha = 5^{\mathrm{o}}$

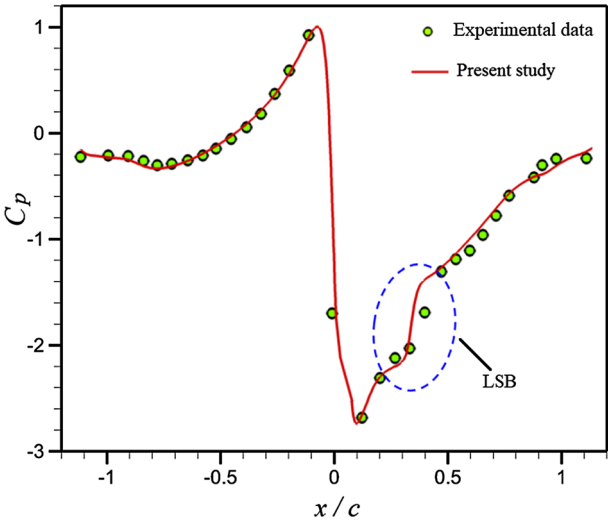

Fig. 5 Comparison of the pressure coefficient of an elliptical cylinder of axis ratio 1:3 with experimental data at $\mathrm{Re} = 1.25 \times 10^5$ and $\alpha = 15^{\mathrm{o}}$

shows two close-up views of the grid. The depth of the cylinder is considered as 0.1 chord length. The boundary conditions are similar to the two-dimensional domain, as shown in Fig. 3, except that for the lateral boundary surfaces in the transverse direction (normal to the z-axis) the periodic condition is applied. The subgrid-scale turbulence models in Ansys fluent software use the Boussinesq hypothesis as follows:

$$\tau_{\mathrm{ij}} = -2\mu_{\mathrm{t}}\overline{S}_{\mathrm{ij}} + \frac{1}{3}\tau_{\mathrm{kk}}\delta_{\mathrm{ij}} \tag{16}$$

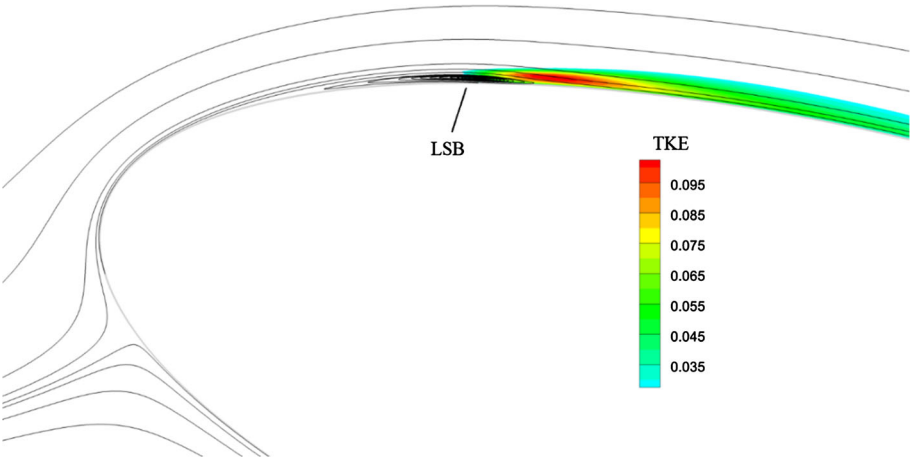

Fig. 6 Contours of TKE near the transition point and LSB form for an elliptical cylinder of axis ratio 1:3 at $\mathrm{Re} = 1.25 \times 10^5$ and $\alpha = 15^o$

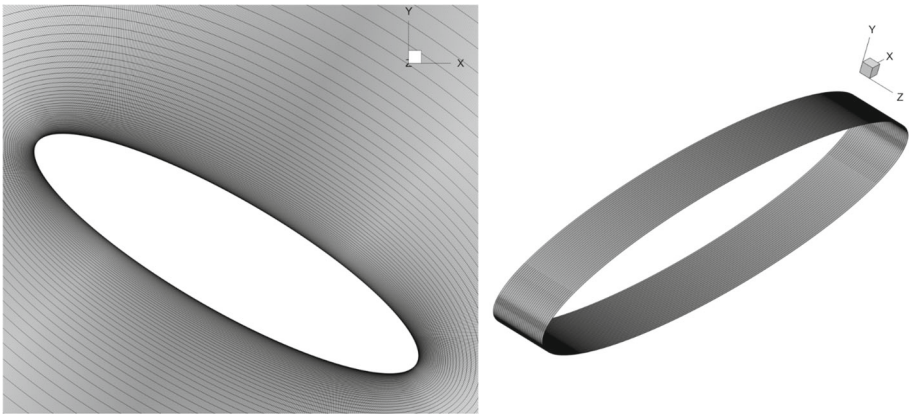

Fig. 7 Computational grid used for LES with $2000 \times 180 \times 50$ points

where μ_t and $\overline{S}_{ij}$ denote the subgrid-scale turbulent viscosity and strain rate tensor, respectively. To model the turbulent viscosity in this study, the wall-adapting local eddy viscosity (WALE) model is utilized [40]. The advantage of this model is to accurately simulate the laminar to turbulent flow transition [41].

Figure 8 depicts the comparison of the pressure coefficient between the LES and the present solver results at $\alpha = 30°$, $\mathrm{Re} = 10^5$, axis ratio of 0.25, and $k = 2$. The maximum value of y + in this simulation is about 1. It seems that the two-dimensional assumption is acceptable. The formation of an LSB is also observed in the figure. One of the useful methods to indicate the turbulent eddies is Q-criterion proposed by Hunt et al. [42]. This criterion defines a vortex as a connected fluid region. Moreover, the Q-criterion represents a local balance between shear strain rate and vorticity magnitude. The contours of the Q-criterion for the above test case are shown in Fig. 9. As shown in the figure, the variations on the transitional region increase. The yellow and red colors indicate the lower and higher values of the Q-criterion, respectively.

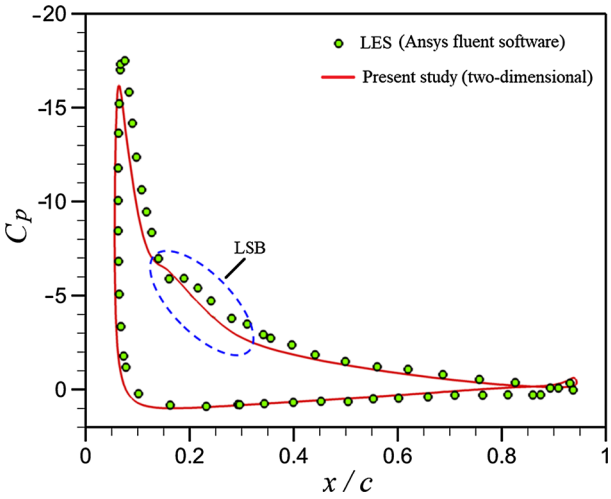

Fig. 8 Comparison of pressure coefficient of the elliptical moving belt between the LES and the present solver results at $\alpha = 30°$, $\mathrm{Re} = 10^5$, and $k = 2$

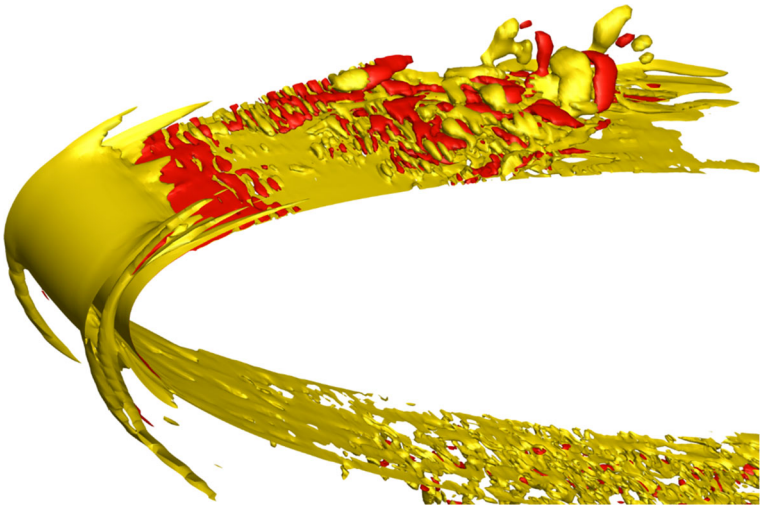

Fig. 9 Contours of Q-criterion near the transitional region obtained by LES at $\alpha = 30°$, $\mathrm{Re} = 10^5$, and $k = 2$

4.2 Analysis of transitional flow around a stationary elliptical belt

To analyze the transitional flow, laminar separation bubble (LSB), and stall conditions, the flow past a stationary elliptical belt with an axis ratio of 0.25 at four angles of attack is investigated. Figure 10 shows the streamlines and contours of turbulent kinetic energy at $\alpha = 5°$, 10°, 15°, and 18°. At $\alpha = 5°$, the bubble is formed on the upper right half of the belt, and on the left half, the flow remains laminar. At $\alpha = 10°$ and 15°, the bubble is located near the leading edge. Therefore, on the belt's upper surface, the turbulent flow is established, which leads to the reattachment of the flow behind the bubble. At $\alpha = 18°$, the bubble bursts, and a long bubble is formed, leading to the belt stall's occurrence. Figure 11 shows the pressure coefficient distributions for the above-mentioned angles of attack. The transition point and the stall occurrence can be observed in the figure.

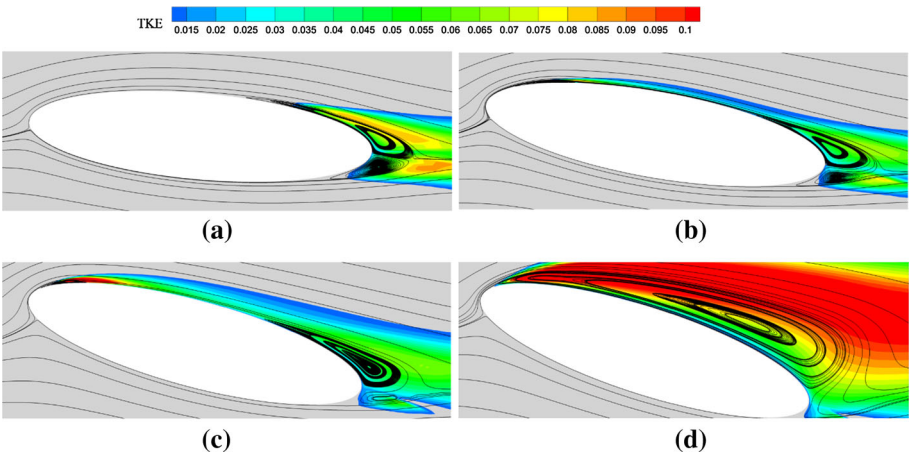

Fig. 10 Streamlines and contours of turbulent kinetic energy for stationary elliptical belt at Re $= 10^5$ **a** $\alpha =$ 5°, **b** $\alpha = 10°$, **c** $\alpha = 15°$, **d** $\alpha = 18^o$

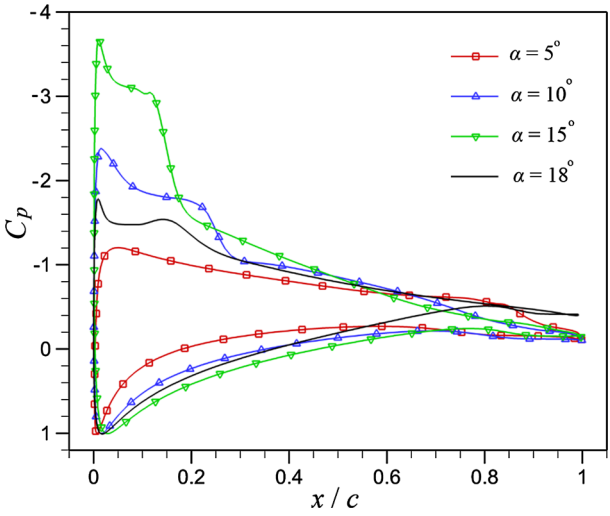

Fig. 11 Pressure coefficient distributions for the stationary elliptical belt at Re $= 10^5$ **a** $\alpha =$ 5°, **b** $\alpha = 10°$, **c** $\alpha = 15°$, **d** $\alpha = 18^o$

4.3 Investigation of aerodynamic characteristics of the belt configurations

As mentioned earlier, the moving belt mechanism generates a lift force due to the Magnus effect. Moreover, it can delay the flow separation by increasing the flow momentum into the wall boundary layer. Therefore, at a given Reynolds number, the lift and drag coefficients of a moving belt are a function of the angle of attack and belt speed. A comparison between the three configurations of the stationary belt (baseline), half belt, and the full belt is made to investigate the belt motion effect on the aerodynamic performances. For this purpose, the lift and drag coefficients of the moving belt with respect to the attack angle at four speed ratios of $k = 0.5$, 1, 1.5, and 2 at Re $= 10^5$ are studied. As shown in Fig. 12, in half and full belts motion, as the speed ratio increases, the lift coefficient is enhanced, and the drag coefficient decreases. A sharp increase of the drag coefficient is seen after the stall occurrence in all the speed ratios. However, at $k = 1.5$ and 2 the decrease of the lift coefficient is gradual because

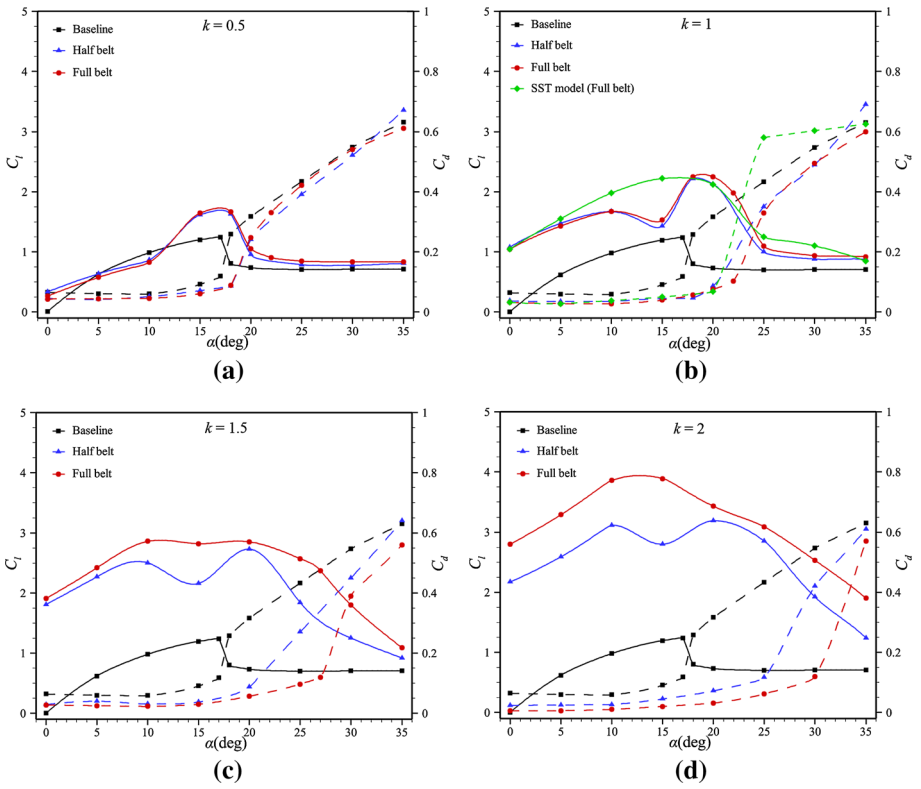

Fig. 12 Comparison of the lift (solid line) and drag coefficients (dashed line) between the baseline, half belt, and full belt configurations at different speed ratios: **a** $k = 0.5$, **b** $k = 1$, **c** $k = 1.5$, and **d** $k = 2$

of the additional momentum effects. Moreover, at $\alpha = 35°$ the lift and drag coefficients of the three cases are almost close. In fact, at higher angles of attack, the belt motion does not affect these coefficients because of the flow separation dominance. For $k \geq 1$ in half belt cases, the lift coefficient at $\alpha = 15°$ is less than at $\alpha = 10°$ due to the change in the vortex structure at the trailing edge. This leads to increasing the pressure on the trailing edge of the upper surface at $\alpha = 15°$. In addition, a significant increase in the lift coefficient is observed in these cases for $15° \leq \alpha \leq 20°$ due to the transition from laminar to turbulent flow on the upper surface. Figure 13 compares the half belt's TKE contours between two angles of attack 15° and 20° at $k = 1.5$. At $\alpha = 15°$, the flow around the belt is completely laminar, while at $\alpha = 20°$, the flow on the upper surface is turbulent, leading to increasing the flow momentum. This momentum reduces the pressure on the upper surface and consequently increases the lift coefficient. Therefore, the lift coefficient of the laminar flow is lower than that of the turbulent flow. To clarify the turbulence intensity effect on the aerodynamic coefficients, a comparison of the lift and drag coefficients between the results obtained from the present transitional model and the fully turbulent *SST k-w* model is performed for the full belt case at $k = 1$. As shown in Fig. 12 (b), for $5° < \alpha < 18°$ the k-k_L-ω and *SST k-w* models show the different lift coefficients due to the different flow regimes. Moreover, the drag coefficients for $\alpha > 20°$ dramatically increase in the *SST* model.

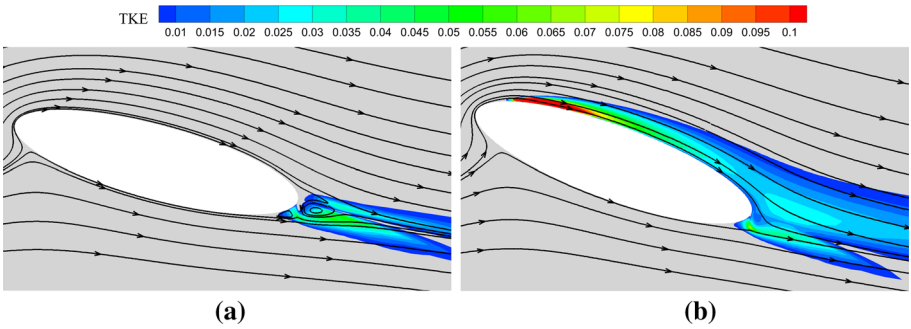

Fig. 13 Contours of turbulent kinetic energy for half belt at $k = 1.5$ and **a** $\alpha = 15°$, **b** $\alpha = 20^{o}$

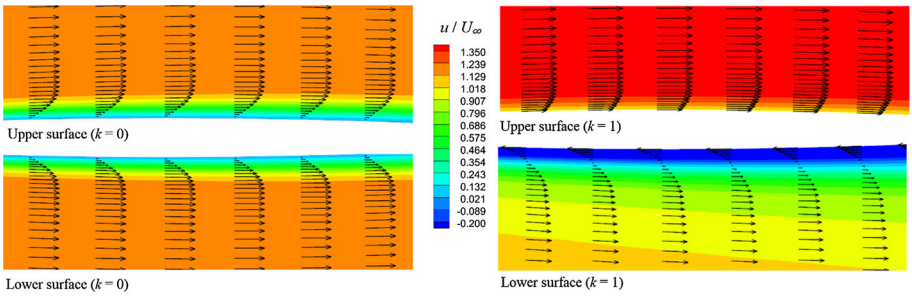

Fig. 14 Vectors and contours of velocity for elliptical belt at $\alpha = 0°$, $k = 0$ (left), and $k = 1$ (right)

The results at $\alpha = 0°$ reveal that the Magnus effect has a significant role in increasing the lift coefficient so that the lift coefficient of $k = 2$ at $\alpha = 0°$ is higher than that of all the angles of attack for $k \leq 1.5$.

By considering the results shown in Fig. 12, the full belt configuration has a better aerodynamic performance compared to the half belt. The continuation of the present study examines the results of the full belt configuration.

4.4 Analysis of flow field around full belt configuration

When the elliptical belt is stationary, the velocity gradient near the solid surface makes a boundary layer. But as the belt moves (as shown in Fig. 1a), the velocity variation at the belt's upper surface decreases and at the lower surface increases. Figure 14 depicts the vectors and contours of velocity for the upper and lower elliptical belt surfaces at $\alpha = 0°$ and $k = 0$, 1. The boundary layer thickness on the upper surface of the moving belt ($k = 1$) decreases compared with the stationary belt ($k = 0$), while on the lower surface of the moving belt, the boundary layer grows. Furthermore, since the direction of the belt motion and the free stream on the lower surface are opposite, the flow fluctuations increase and cause turbulence of the flow, as shown in Fig. 15. This figure shows the contours of laminar kinetic energy (LKE) near the solid surface, which indicates the onset of transition in the laminar boundary layer.

In order to evaluate the effect of the angle of attack on the transition onset of the moving belt, the contours of LKE are plotted for several angles of attack at $k = 1$, as shown in Fig. 16. Arrows in the figure indicate the points of transition onset. At $\alpha = 0^{o}$, and 10°, the flow on the lower surface is turbulent, while on the upper surface, the flow is still laminar. At $\alpha = 20°$

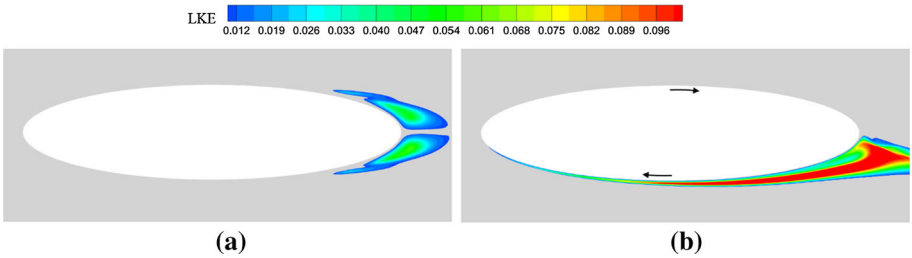

Fig. 15 Contours of laminar kinetic energy for elliptical belt at $\alpha = 0°$ and **a** $k = 0$, **b** $k = 1$

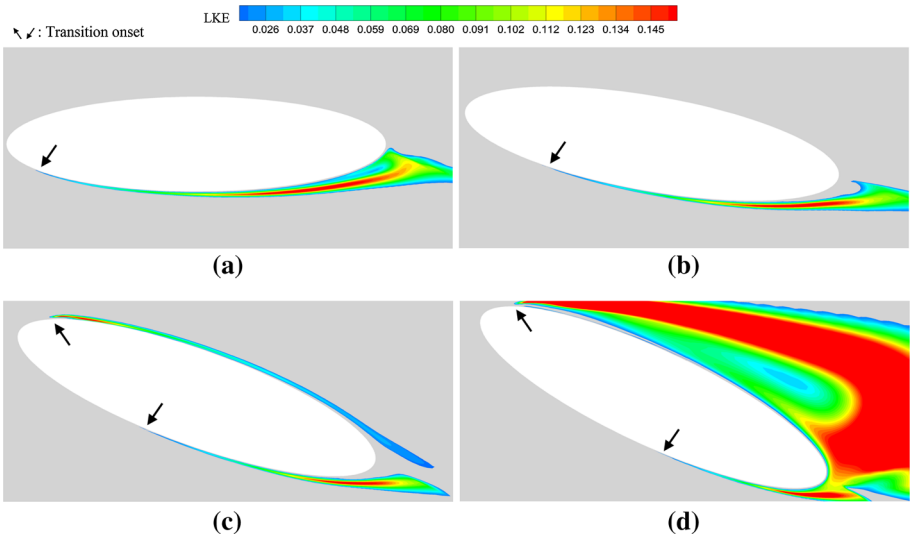

Fig. 16 Contours of LKE with transition onset for elliptical belt at $k = 1$ **a** $\alpha = 0°$, **b** $\alpha = 10°$, **c** $\alpha = 20°$, **d** $\alpha = 25°$

and 25°, the entire upper surface and a part of the lower surface experience the turbulent flow. Moreover, as the attack angle increases, the transition onset on the lower surface of the belt delays due to the flow deceleration. Figure 15 depicts the skin friction distributions at $k = 1$ and $\alpha = 0°$, 10°, 20°, and 25°. The transition from laminar to turbulent flow causes an increase in the skin friction coefficient due to the increase in the velocity gradient near the wall. As can be seen in Figs. 17c and d, the turbulence intensity on the upper surface (where the separation bubbles form) is higher than the lower surfaces of the belt because the bubble makes more fluctuations. Moreover, a comparison with the SST k-ω turbulence model is performed at $\alpha = 10°$ and 25° in Fig. 15. The SST k-ω model could not capture the LSB because of the fully turbulent treatment of this model. However, there is not a significant difference between the skin friction coefficients at $\alpha = 10°$. At $\alpha = 25°$, the skin friction obtained by the SST model is more than that of the k-k_L-ω model on the lower surface because the flow simulated by the k-k_L-ω model is laminar up to $x/c = 0.6$.

A comparison between Fig. 10b and 16b at $\alpha = 10°$ indicates that only the upper surface encounters the turbulent flow for the stationary belt. In contrast, for the moving belt, on the upper surface, the flow is laminar, and on the lower surface, the turbulence is formed. Furthermore, the stationary belt stalls at $\alpha = 18°$, while on the moving belt, a short separation

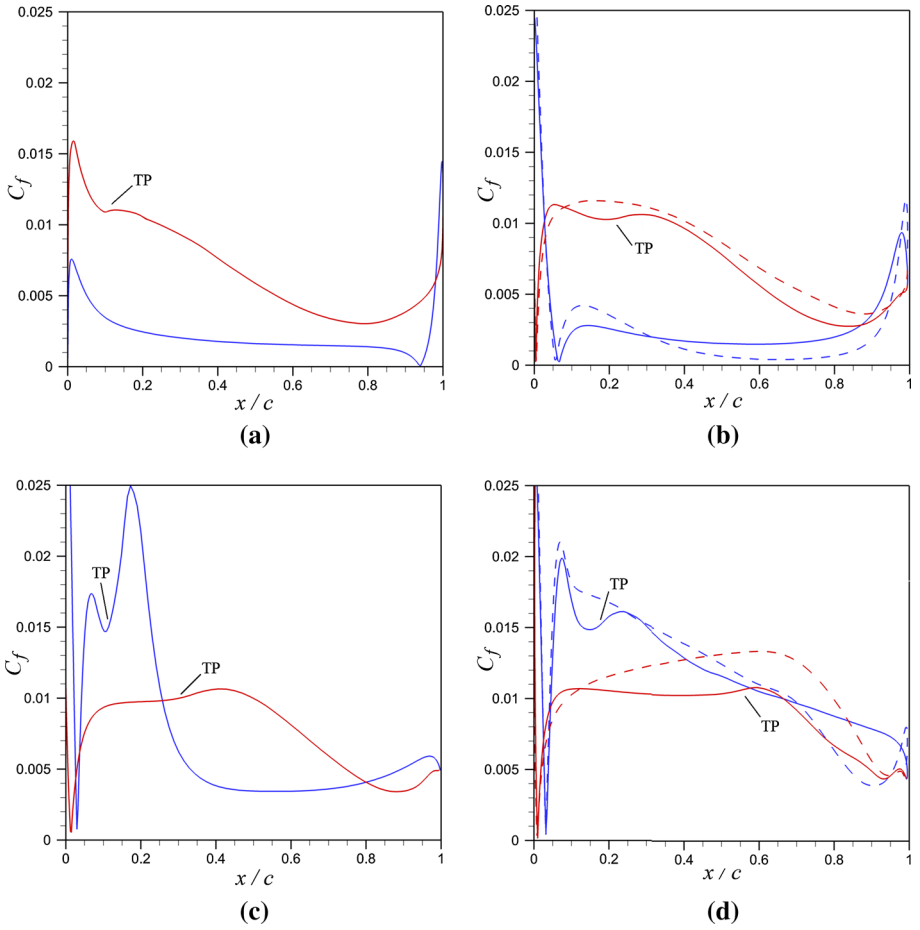

Fig. 17 Skin friction distributions for elliptical belt at $k = 1$, **a** $\alpha = 0°$, **b** $\alpha = 10°$, **c** $\alpha = 20°$, **d** $\alpha = 25°$. Blue line: upper surface, red line: lower surface, dashed: SST k-ω turbulence model

bubble is formed at this angle of attack. In fact, the belt motion injects sufficient momentum into the boundary layer, leading to avoiding the LSB burst.

Figure 18 shows the streamlines and contours of turbulent kinetic energy at $\alpha = 20°$, and $k = 0$, 1, and 2. At the stationary belt ($k = 0$), a long separation bubble is observed, which indicates the stall occurrence. At $k = 1$, the stall is suppressed due to the momentum injection, and a small bubble is formed. At $k = 2$, a non-separated flow is seen, and the small LSB is disappeared. Moreover, at $k = 0$, the flow near the lower surface is laminar, while at $k = 2$, the flow on the entire lower surface is turbulent.

In addition to the issue of the flow transition, it can also be important to examine the formation of the separation bubble of the flow around the elliptical belt. For the cases studied in the present paper, three types of flow patterns are formed in terms of the leading-edge separation: without leading-edge bubble, with leading-edge bubble, and with long bubble (stall situation). Figure 19 shows the classification of the flow patterns around the elliptical belt. For the low-speed ratios, in a larger part of the study area, the flow includes the long bubble. By increasing the speed ratio, the momentum injected into the surface boundary layer

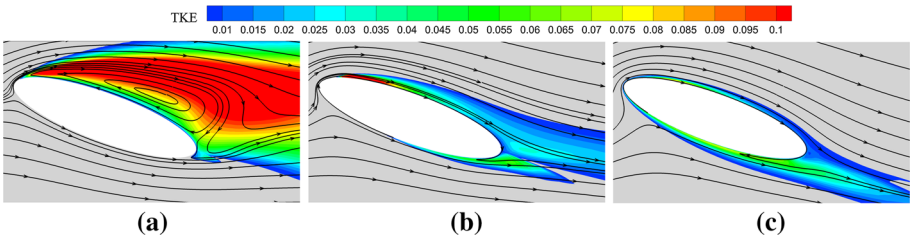

Fig. 18 Streamlines and contours of turbulent kinetic energy for moving elliptical belt at $\alpha = 20°$ and **a** stationary belt ($k = 0$), **b** $k = 1$, **c** $k = 2$

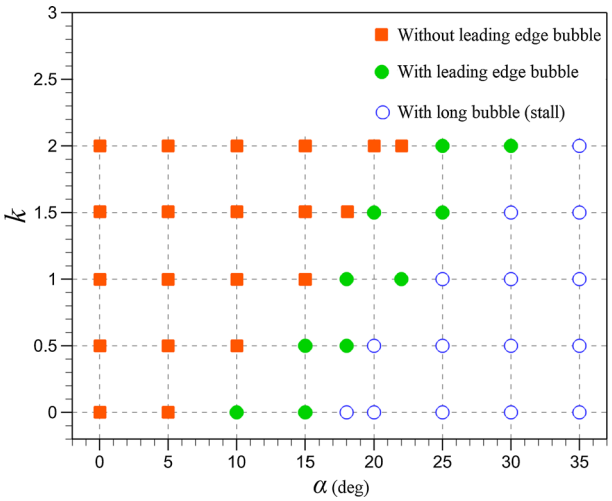

Fig. 19 Flow patterns around the elliptical belt

increases, which causes the increase in the stall angle so that at $k = 0$, 0.5, 1, 1.5, and 2, the stall angle is 15°, 18°, 22°, 25°, and 30°, respectively. In all the speed ratios, the leading-edge LSB (green circles) is formed in a small range of attack angles.

5 Discussions

LSB may be short or long, depending on the correction of the corresponding pressure distribution [43]. Changes in flow parameters may cause the bubble to pass abruptly from short to long, which is called the bursting of the bubble occurs [44]. LSBs are generally acknowledged as a disturbing factor that leads to increased drag and decreases aerodynamic efficiency [45]. Furthermore, they are sensitive to small fluctuations of upstream flow characteristics and cause instability. This instability, in addition to reducing the aerodynamic performance, poses a risk of aerodynamic structure damage [46]. Therefore, the use of methods to control and eliminate LSB is an essential issue and has attracted the attention of many researchers. Synthetic jet [47], vortex generator [48], co-flow jet [49, 50], and moving surfaces [26, 27] are some examples of flow control methods. Each of the flow control methods can be used according to the operating conditions of the aerodynamic vehicles. The present study focuses on the use of the moving surface and the work that has been done in this field, as well as

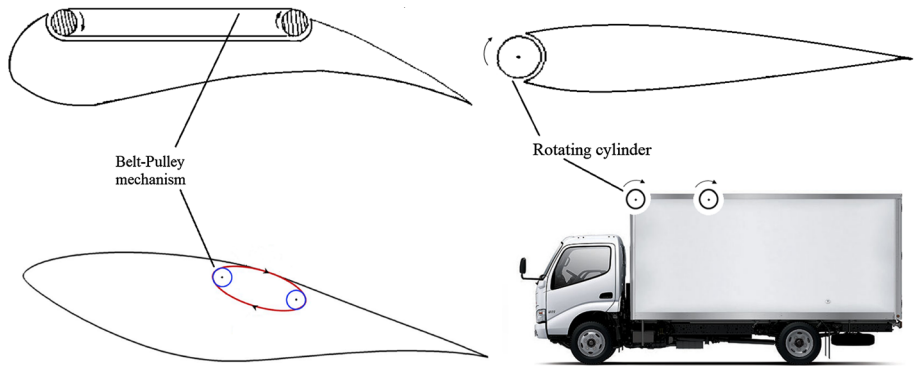

Fig. 20 Schematics of moving surface applications

new ideas that can be used in this direction. Figure 20 shows the different applications of moving belts [19, 27] and rotating cylinders [51]. The moving surface method is known as a mechanism to increase the lift coefficient and decrease the drag coefficient [52]. Hence, to improve the aerodynamic performances, this method can be used in aero-vehicles and wind turbine blades.

Modi [51] experimentally and numerically studied the moving surface boundary layer control. For this purpose, a rotating cylinder was located in the leading edge, trailing edge, and an upper surface of an airfoil. The results showed that using this method delays the stall angle, reduces the drag, and increases the lift coefficient. Salimipour and Yazdani [27] numerically investigated the effect of a moving surface on the performance of a horizontal axis wind turbine. The innovation of their work is to find the best location of the moving surface and its speed in different sections of the turbine's blade, as well as calculating the power consumption requirements. In an experimental study, Boukenkoul et al. [25] placed a moving belt on the upper surface of an airfoil and investigated the effect of belt speed on aerodynamic performance. In the present study, the belt is placed around the entire geometry; however, in Refs. [27] and [51] the belt is used only in a part of the geometry. Table 2 compares the mechanical performance ratio (η / η_{Baseline}) between the present work and the above-mentioned studies. In the available speed ratios and angles of attack, the results of this study show a better performance than that of the two other references. In addition to the reason mentioned, the present results show a better performance in all the attack angles compared to Ref. [25] due to the use of a transitional flow regime.

6 Conclusions

In the current work, the flow past an elliptical moving belt at the ellipse axis ratio of 0.25 and Reynolds number of 10^5 was numerically studied using a finite-volume pressure-based scheme. An in-house code was developed to numerically solve the Reynolds-averaged Navier–Stokes equations and three-equation transitional turbulence model. Two configurations of full belt and half belt were considered. A wide range of attack angles ($0° \leq \alpha \leq 30°$) and speed ratio ($0 \leq k \leq 2$) was considered. The results showed that the full belt configuration had a better aerodynamic performance compared to the half belt.

Moreover, the moving belt caused the reduction of boundary layer thickness on the upper surface of the belt. Since the direction of the full belt motion and the free stream on the

Table 2 $\eta/\eta_{\text{Baseline}}$ for various speed ratios

α (deg) k	5	10	15	20	25	30	35	
0.5	1.25	0.88	1.98	1.81	1.24	1.17	1.16	Present study
1	4	2.76	2.25	10.8	1.97	1.44	1.61	Present study
	1.3	1.27	1.84	–	–	–	–	Ref. [27]
	2.1	0.92	1.15	1.5	1.15	1.0	1.0	Ref. [51]
1.5	4.68	3.9	7.15	12.8	11.8	3.25	1.65	Present study
2	7.76	4.47	3.89	17.42	15.81	10.4	1.71	Present study
	4.5	2.0	1.75	1.5	1.5	1.55	1.9	Ref. [25]
	1.28	1.25	2.21	–	–	–	–	Ref. [27]

lower surface was opposite, the flow fluctuations increased and led to an increase in the flow turbulence near the surface. At $k = 1$ and $0° \leq \alpha \leq 10°$, the flow on the lower surface was turbulent, while on the upper surface, the flow was still laminar. For $20° \leq \alpha \leq 25°$, the flow near the upper surface was completely turbulent. Moreover, by increasing the angle of attack, the transition onset on the lower surface of the full belt is delayed. Furthermore, as the speed ratio increased, the stall angle was enhanced. The aerodynamic analysis of the elliptical moving belt exposed to the free stream showed that the belt motion increased the lift coefficient and decreased the drag coefficient. The results at $\alpha = 0°$ indicated that the Magnus effect had a significant role in enhancing the lift coefficient.

References

1. S. Mittal, B. Kumar, Flow past a rotating cylinder. J. Fluid Mech. **476**, 303–334 (2003). https://doi.org/10.1017/s0022112002002938
2. J.O. Pralits, L. Brandt, F. Giannetti, Instability and sensitivity of the flow around a rotating circular cylinder. J. Fluid Mech. **650**, 513–536 (2010). https://doi.org/10.1017/s0022112009993764
3. J.O. Pralits, F. Giannetti, L. Brandt, Three-dimensional instability of the flow around a rotating circular cylinder. J. Fluid Mech. **730**, 5–18 (2013). https://doi.org/10.1017/jfm.2013.334
4. A. Rao, A. Radi, J.S. Leontini, M.C. Thompson, J. Sheridan, K. Hourigan, A review of rotating cylinder wake transitions. J. Fluids Struct. **53**, 2–14 (2015). https://doi.org/10.1016/j.jfluidstructs.2014.03.010
5. E. Salimipour, M. Anbarsooz, Surface temperature effects on the compressible flow past a rotating cylinder. Phys. Fluids **31**(2), 023601 (2019). https://doi.org/10.1063/1.5082162
6. A.R. Teymourtash, S.E. Salimipour, Compressibility effects on the flow past a rotating cylinder. Phys. Fluids **29**(1), 016101 (2017). https://doi.org/10.1063/1.4973564
7. R. Mittal, S. Balachandar, Direct Numerical Simulation of Flow Past Elliptic Cylinders. J. Comput. Phys. **124**(2), 351–367 (1996). https://doi.org/10.1006/jcph.1996.0065
8. W.A. Khan, R.J. Culham, M.M. Yovanovich, Fluid flow around and heat transfer from elliptical cylinders: analytical approach. J. Thermophys. Heat Transfer **19**(2), 178–185 (2005). https://doi.org/10.2514/1.10456
9. I. Paul, K.A. Prakash, S. Vengadesan, Onset of laminar separation and vortex shedding in flow past unconfined elliptic cylinders. Phys. Fluids (2014). https://doi.org/10.1063/1.4866454
10. I. Paul, K. Arul Prakash, S. Vengadesan, Numerical analysis of laminar fluid flow characteristics past an elliptic cylinder. Int. J. Numer. Methods Heat Fluid Flow **24**(7), 1570–1594 (2014). https://doi.org/10.1108/hff-10-2012-0225
11. M.C. Thompson, A. Radi, A. Rao, J. Sheridan, K. Hourigan, Low-Reynolds-number wakes of elliptical cylinders: from the circular cylinder to the normal flat plate. J. Fluid Mech. **751**, 570–600 (2014).
12. R. Subburaj, P. Khandelwal, S. Vengadesan, Numerical study of flow past an elliptic cylinder near a free surface. Phys. Fluids (2018). https://doi.org/10.1063/15046745

13. M.J. Ezadi Yazdi, A. Bak Khoshnevis, Experimental study of the flow across an elliptic cylinder at subcritical Reynolds number. Eur. Phys. J. Plus (2018). https://doi.org/10.1140/epjp/i2018-12342-1
14. H. Jiang, L. Cheng, S. Draper, H. An, Two- and three-dimensional instabilities in the wake of a circular cylinder near a moving wall. J. Fluid Mech. **812**, 435–462 (2017). https://doi.org/10.1017/jfm.2016.810
15. S.N. Naik, S. Vengadesan, K.A. Prakash, Numerical study of fluid flow past a rotating elliptic cylinder. J. Fluids Struct. **68**, 15–31 (2017). https://doi.org/10.1016/j.jfluidstructs.2016.09.011
16. S.N. Naik, S. Vengadesan, K. Arul Prakash, linear shear flow past a rotating elliptic cylinder. J. Fluids Eng. (2018). https://doi.org/10.1115/14040365
17. H. Lu, K.B. Lua, T.T. Lim, Flow past a rapidly rotating elliptic cylinder. Eur. J. Mech. B. Fluids **72**, 676–690 (2018). https://doi.org/10.1016/j.euromechflu.2018.08.011
18. J. Zhu, L.E. Holmedal, D. Myrhaug, H. Wang, Near-wall effect on flow around an elliptic cylinder translating above a plane wall. Phys. Fluids (2020). https://doi.org/10.1063/50020818
19. A. Favre, *Contribution a l'étude expérimentale des mouvements hydrodynamiques à deux dimensions* ([France] Ministère de l'air. Publications scientifiques et techniques). Paris, E. Blondel La Rougery, 1938.
20. F. Moktarian, V.J. Modi, Fluid dynamics of airfoils with moving surface boundary-layer control. J. Aircr. **25**(2), 163–169 (1988). https://doi.org/10.2514/3.45557
21. V.J. Modi, F. Mokhtarian, M.S.U.K. Fernando, T. Yokomizo, Moving surface boundary-layer control as applied to two-dimensional airfoils. J. Aircr. **28**(2), 104–112 (1991). https://doi.org/10.2514/3.45998
22. V.J. Modi, Moving Surface Boundary-Layer Control: A Review. J. Fluids Struct. **11**(6), 627–663 (1997). https://doi.org/10.1006/jfls.1997.0098
23. V.J. Modi, E. Shih, B. Ying, T. Yokomizo, Drag reduction of bluff bodies through momentum injection. J. Aircr. **29**(3), 429–436 (1992). https://doi.org/10.2514/3.46179
24. L. Li, "Numerical Investigation on Flow Control with Moving Surface Over a NACA0015 Airfoil". In *Advances in Effective Flow Separation Control for Aircraft Drag Reduction*, (Computational Methods in Applied Sciences, 2020, ch. Chapter 11, pp. 205–215.
25. M.A. Boukenkoul, F.-C. Li, W.-L. Chen, H.-N. Zhang, Lift-generation and moving-wall flow control over a low aspect ratio airfoil. J. Fluids Eng. (2018). https://doi.org/10.1115/14037681
26. E. Salimipour, A. Salimipour, Power minimization and vortex shedding elimination of a circular cylinder by moving surface mechanism. Ocean Eng. (2019). https://doi.org/10.1016/j.oceaneng.2019.106408
27. E. Salimipour, S. Yazdani, Improvement of aerodynamic performance of an offshore wind turbine blade by moving surface mechanism. Ocean Eng. (2020). https://doi.org/10.1016/j.oceaneng.2019.106710
28. J.S. Samuthira Pandi, S. Mittal, Wake transitions and laminar separation bubble in the flow past an Eppler 61 airfoil. Phys. Fluids (2019). https://doi.org/10.1063/15113823
29. H. Fadhila, H. Medina, S. Aleksandrova, S. Benjamin, A new non-linear RANS model with enhanced near-wall treatment of turbulence anisotropy. Appl. Math. Model. **82**, 293–313 (2020). https://doi.org/10.1016/j.apm.2020.01.056
30. Z. Malikov, Mathematical model of turbulence based on the dynamics of two fluids. Appl. Math. Model. **82**, 409–436 (2020). https://doi.org/10.1016/j.apm.2020.01.047
31. L. Shi, Y. Wang, G. Zhang, Y. Jin, D. Zhang, Assessment of an improved turbulence model in simulating the unsteady flows around a D-shaped cylinder and an open cavity. Appl. Math. Model. **83**, 552–575 (2020). https://doi.org/10.1016/j.apm.2020.01.068
32. E. Salimipour, A modification of the k-kL-ω turbulence model for simulation of short and long separation bubbles. Comput. Fluids **181**, 67–76 (2019). https://doi.org/10.1016/j.compfluid.2019.01.003
33. V.A. Aleksin, S.V. Utyuzhnikov, Implementation of near-wall boundary conditions for modeling boundary layers with free-stream turbulence. Appl. Math. Model. **38**(14), 3591–3606 (2014). https://doi.org/10.1016/j.apm.2013.11.066
34. E. Salimipour, A numerical study on the fluid flow and heat transfer from a horizontal circular cylinder under mixed convection. Int. J. Heat Mass Transf. **131**, 365–374 (2019). https://doi.org/10.1016/j.ijheatmasstransfer.2018.11.084
35. H. Medina, J. Early, Modelling transition due to backward-facing steps using the laminar kinetic energy concept. Eur. J. Mech. B. Fluids **44**, 60–68 (2014). https://doi.org/10.1016/j.euromechflu.2013.10.004
36. M. Lee, G. Park, C. Park, C. Kim, W. Tangchirapat, Improvement of grid independence test for computational fluid dynamics model of building based on grid resolution. Adv. Civil Eng. (2020). https://doi.org/10.1155/2020/8827936
37. E. Salimipour, Thermal buoyancy effects on the flow field and heat transfer of a rotating cylinder: A numerical study. Int. J. Thermal Sci. (2020). https://doi.org/10.1016/j.ijthermalsci.2020.106453
38. P. Ziadé, M.A. Feero, P. Lavoie, P.E. Sullivan, Shear layer development, separation, and stability over a low-reynolds number airfoil. J. Fluids Eng. **140**(7), 071201 (2018). https://doi.org/10.1115/1.4039233

39. T. Ota, H. Nishiyama, Y. Taoka, Flow around an elliptic cylinder in the critical reynolds number regime. J. Fluids Eng. **109**(2), 149–155 (1987). https://doi.org/10.1115/1.3242635
40. H.Y. Cheng, X.R. Bai, X.P. Long, B. Ji, X.X. Peng, M. Farhat, Large eddy simulation of the tip-leakage cavitating flow with an insight on how cavitation influences vorticity and turbulence. Appl. Math. Model. **77**, 788–809 (2020). https://doi.org/10.1016/j.apm.2019.08.005
41. A.C.Y. Yuen, G.H. Yeoh, V. Timchenko, S.C.P. Cheung, T. Chen, Study of three LES subgrid-scale turbulence models for predictions of heat and mass transfer in large-scale compartment fires. Numer. Heat Transfer, Part A: Appl. **69**(11), 1223–1241 (2016). https://doi.org/10.1080/10407782.2016.1139903
42. J. C. R. Hunt, A. A. Wray, and P. Moin, *Eddies, stream, and convergence zones in turbulent flows*. Center for Turbulence Research Report CTR-S88, 1988.
43. C.E. Toppings, J.W. Kurelek, S. Yarusevych, Laminar separation bubble development on a finite wing. AIAA J. (2021). https://doi.org/10.2514/1J060258
44. E. Eljack, J. Soria, Y. Elawad, T. Ohtake, Simulation and characterization of the laminar separation bubble over a NACA-0012 airfoil as a function of angle of attack. Phys. Rev. Fluids (2021). https://doi.org/10.1103/PhysRevFluids.6.034701
45. X. Zhang, K.-S. Choi, Y. Huang, H.-X. Li, Flow control over a circular cylinder using virtual moving surface boundary layer control. Experiments Fluids (2019). https://doi.org/10.1007/s00348-019-2745-y
46. S.J. Schreck, M.C. Robinson, Horizontal axis wind turbine blade aerodynamics in experiments and modeling. IEEE Trans. Energy Convers. **22**(1), 61–70 (2007). https://doi.org/10.1109/tec.2006.889620
47. A. Abbasi, S. Yazdani, A numerical investigation of synthetic jet effect on dynamic stall control of oscillating airfoil. Scientia Iranica (2019). https://doi.org/10.24200/sci.2019.52743.2870
48. S.S.M. Jafroudi, N. Amanifard, H.M. Deylami, Heat transfer enhancement through a rectangular channel by DBD plasma actuators as vortex generators. Eur. Phys. J. Plus (2021). https://doi.org/10.1140/epjp/s13360-021-01499-5
49. A. Bak Khoshnevis, S. Yazdani, E. Salimipour, Effects of CFJ flow control on aerodynamic performance of symmetric NACA airfoils. J. Turbul. **21**(12), 704–721 (2020)
50. A. Khoshnevis, S. Yazdani, E. Saimipour, Analysis of co-flow jet effects on airfoil at moderate Reynolds numbers. J. Theor. Appl. Mech. **58**(3), 685–695 (2020). https://doi.org/10.15632/jtam-pl/122266
51. V. Modi, On the moving surface boundary-layer control, presented at the Fluids 2000 Conference and Exhibit, 2000.
52. J.C. Schulmeister, J.M. Dahl, G.D. Weymouth, M.S. Triantafyllou, Flow control with rotating cylinders. J. Fluid Mech. **825**, 743–763 (2017). https://doi.org/10.1017/jfm.2017.395